Communications Earth & Environment https://doi.org/10.1038/s43247-026-03654-1

Article in Press

Sediment records reveal elevated black carbon emissions potentially amplifying Arctic snowmelt

Received: 7 January 2026

Accepted: 11 May 2026

Cite this article as: Gong, X., Han, Y., Zhu, C. *et al.* Sediment records reveal elevated black carbon emissions potentially amplifying Arctic snowmelt. *Commun Earth Environ* (2026). https://doi.org/10.1038/s43247-026-03654-1

Xuehong Gong, Yongming Han, Chongshu Zhu, Tzung-May Fu, Qiyuan Wang, Dewen Lei, Jiaoyang Yu, Ruonan Wang, Zhisheng An & Guohui Li

Sediment records reveal elevated black carbon emissions potentially amplifying Arctic snowmelt

Xuehong Gong[1,2], Yongming Han[1,3*], Chongshu Zhu[1], Tzung-May Fu[4], Qiyuan Wang[1], Dewen Lei[5], Jiaoyang Yu[1], Ruonan Wang[1], Zhisheng An[1,2], Guohui Li[1*]

[1] State Key Laboratory of Loess Science, Institute of Earth Environment, Chinese Academy of Sciences, Xi'an 710061, China
[2] State Key Laboratory of Earth Surface Processes and Hazards Risk Governance, Faculty of Geographical Science, Beijing Normal University, Beijing 100875, China
[3] School of Human Settlements and Civil Engineering, Xi'an Jiaotong University, Xi'an 710049, China
[4] School of Environmental Science and Engineering, Southern University of Science and Technology, Shenzhen 518055, China
[5] China Institute of Geo-Environment Monitoring, Beijing 100081, China

Correspondence to: Yongming Han and Guohui Li (yongming@ieecas.cn and ligh@ieecas.cn)

Abstract. Black carbon, an important component of atmospheric aerosols, has an impact on climate change. When deposited on snow and ice, it reduces surface albedo, accelerating melting and amplifying global warming. Here we analyzed lake sediment records from China and found that existing bottom-up inventories underestimate black carbon emissions prior to the mid-twentieth century. We incorporated a black carbon emission enhancement scheme based on reconstructed historical biomass burning emissions into a numerical climate model to assess this underestimation. The simulations indicated that increased historical emissions enhanced spring and summer radiative effects north of 60°N, leading to regional surface warming and accelerated Arctic snowmelt. Although the response varies with the strength of emission enhancement, the findings suggested that historical BC emission biases could alter the simulated Arctic energy balance and climate evolution. These results highlight the need for improved constraints on historical BC emissions to better assess their climate impacts.

Introduction

Black carbon (BC) is a highly light-absorbing component of atmospheric fine particulate matter ($PM_{2.5}$), primarily produced by the incomplete combustion of fossil fuels, biofuels, and biomass[1–5]. BC not only directly changes the radiation balance of the Earth's climate system but also indirectly affects global or regional climate by altering the microphysical properties of clouds through serving as cloud condensation nuclei or ice nuclei[6].

Furthermore, the deposition of BC has an impact on the Arctic climate. BC deposited on snow and ice reduces surface albedo and enhances shortwave absorption, thereby accelerating snowmelt and amplifying Arctic warming[7–9]. Arctic responses are not solely impacted by local emissions, changes in BC concentrations outside the Arctic can also influence Arctic climate by altering polar heat transport[10]. Previous studies have shown that an increase in BC emissions in mid-latitude regions causes a rise in Arctic temperatures[11,12], highlighting the importance of understanding both the source regions and transport pathways.

Although considerable progress has been made in quantifying BC radiative forcing, the relevant estimates remain heavily dependent on emission inventories with substantial uncertainties. This is particularly the case for the early 20th century, a period characterized by limited observational data. Currently, most inventories are developed using

bottom-up methods based on fuel consumption statistics and emission factors[1,13,14]. However, the lack of comprehensive historical records, especially regarding residential combustion and small industrial activities, introduces substantial uncertainties[15,16]. Due to the lack of observational constraints on historical BC emissions, many climate modeling studies have used idealized scaling experiments to investigate the interactions between BC emissions and climate[11,17–21]. Although these simulations are effective for diagnosing climate sensitivity to BC, they do not address the potential systematic underestimation of historical BC emissions. If early background BC emission levels were substantially higher than current estimates, the cumulative radiative forcing, particularly in climate-sensitive regions such as the Arctic, may be underestimated.

To address this limitation, independent observational evidence is necessary to constrain the historical BC emissions. Ice-core records from the Greenland ice sheet and high-latitude glaciers provide valuable long-term reconstructions of atmospheric BC, mainly reflecting large-scale and long-range transport signals[22–25]. Lake sediment records from inland regions can capture variations in BC deposition on both regional and local scales. In particular, maar lakes with closed catchments and limited hydrological input mainly record atmospheric deposition, thereby providing regionally representative histories of BC that retain signals of broader atmospheric changes[26,27].

In sedimentary studies, BC forms through two distinct pathways: the condensation of atmospheric volatiles produces highly graphitized soot-BC, whereas the incomplete combustion of solid materials generates char-BC[28–30]. Previous research has clearly delineated the distinction between "char" and "soot"[28–32]. Char usually deposits within a relatively short distance from the emission source, while soot, as submicron-sized particles, can undergo long-range atmospheric transport. Such extensive transport of soot affects global climate dynamics, alters precipitation patterns, and accelerates glacier melt[33–36]. Therefore, soot preserved in lake sediments provides an important archive for reconstructing atmospheric BC emissions associated with long-range atmospheric transport.

BC emitted from East Asia can be transported poleward by the prevailing mid-latitude westerlies, contributing to atmospheric deposition in the Arctic[37–39]. China is one of the major BC source regions in East Asia and has experienced substantial emission growth associated with rapid industrialization since the mid-20th century[40,41]. Consequently, constraining long-term BC emission trends from China is essential for enhancing our understanding of BC transport and its climatic effects in the Arctic.

In this study, we combined lake sediment records and Community Earth System Model version 2 (CESM2) simulations to investigate historical BC deposition across China. Comparisons between soot fluxes from lake sediment records and modeled BC deposition fluxes in CESM2 revealed an underestimation of background BC emissions prior to the mid-20th century. Constrained by sediment records, we introduced a semi-empirical emission correction and reassessed the associated climatic responses. The revised emissions led to stronger radiative perturbations in high latitudes and enhanced snow-albedo feedbacks. These results highlight the importance of accurately constraining early BC emissions for reliably assessing the climatic impacts of BC in climate simulations.

Results and discussion

Reconstructed soot trend in lake sediment records

A variety of methods have been used for BC quantification[30–32,42–44]. In atmospheric aerosol research, BC refers to the refractory and absorptive carbonaceous particles generated by high-temperature combustion of fossil fuels and biomass[1,2]. These particles typically exist as submicron particles and can be transported at regional to hemispheric scales by atmospheric circulation despite their relatively short atmospheric residence time of only a few days[1,45,46]. In sedimentary studies, BC is commonly subdivided into char and soot according to their formation mechanisms and physicochemical properties[29,30]. Char represents solid combustion residues formed at relatively lower temperatures and is generally associated with coarse particle sizes and short atmospheric lifetimes, leading to predominantly local deposition. In contrast, soot consists of highly graphitized particles formed through gas-to-particle condensation at high combustion temperatures and is dominated by submicron fractions that exhibit strong light absorption and efficient regional transport[31,32,45,47].

Han et al.[42] for the first time discriminated char and soot in sediments and soils using the thermal/optical reflectance (TOR) method, the most commonly used method for BC (or EC, elemental carbon) quantification of carbonaceous aerosol samples. The soot fraction identified by this method is generally associated with the fine particle component of BC and shares key physicochemical characteristics with atmospheric BC as represented in aerosol and climate studies. These characteristics include strong light absorption, refractory behavior, and submicron particle size[1,47,48]. Soot in sediments serves as a more physically consistent proxy for atmospheric BC deposition than total BC or char. Inclusion of char would introduce a stronger influence from local combustion, potentially reducing the comparability between sediment records and model-simulated atmospheric BC. Therefore, soot fluxes derived from sediment cores provide a more atmospherically relevant indicator for evaluating BC deposition and its variability.

Sihailongwan Maar Lake (SHLW) is a closed-basin maar lake located in a remote volcanic region of northeastern China, with no river inflow or outflow. The sediment record from SHLW is predominantly derived from atmospheric deposition rather than catchment inputs[27,49]. The lake is surrounded by extensive forest cover and lies in a region of low population density, which minimizes local anthropogenic disturbance (Fig. 1). The regional climate is dominated by the East Asian monsoon system, with southerly winds prevailing in summer and northwesterly winds associated with the Siberian High in winter (Supplementary Fig. S1)[27,50–52]. These circulation patterns place SHLW within large-scale regional atmospheric transport pathways linking northeastern China with broader East Asian continental emission regions.

We reconstructed the soot deposition flux of SHLW Lake from 1900 to 2019 (Fig. 1c-d). Over this period, SHLW Lake's soot fluxes remained relatively stable from 1900 to 1950, ranging between 0.20-0.31 g m^{-2} yr^{-1} (mean 0.25 g m^{-2} yr^{-1}), with no statistically significant linear trend (Fig. 1c-d, Supplementary Fig. S2c and Supplementary Table S1). This suggested relatively stable regional background conditions during this period. After 1950, the soot flux showed a statistically significant increasing trend ($p < 0.01$), peaking at 0.49 g m^{-2} yr^{-1} (mean: 0.36 g m^{-2} yr^{-1}) (Fig. 1c-d, Supplementary Fig. S2c and Supplementary Table S1). Piecewise regression analysis further indicated a significant change in slope before and after 1950 (Δslope, $p < 0.001$) (Supplementary Fig. S2c). Additional fluctuations in the soot fluxes were present over the past decade (Fig. 1c-d). Soot fluxes declined around 2012, broadly consistent with China's strengthened air pollution control policies. A temporary increase was also observed around 2015. This

more likely reflected interannual variability driven by atmospheric transport and regional emissions. In particular, previous studies have reported open burning of agricultural residues increased substantially in northeastern China during the 2010s, which may have temporarily increased soot emissions reaching the region[53].

This trend at SHLW was corroborated by sediment records from other lakes, including Huguangyan (HGY), Nam Co, Qinghai (QH), Gonghai (GH), Yinjia (YJ), Chaohu (CH), and Taihu (TH) (Fig. 2c-i and Supplementary Table S1). Data for these lakes are from previously published studies[26,54–59], as indicated on the map (Fig. 1a). From 1900 to 1950, soot fluxes across these lakes remained generally stable, and the trends at most sites before 1950 were weak or statistically insignificant (Fig. 2, Supplementary Fig. S2 and Supplementary Table S1). In contrast, most lakes exhibited an increasing trend since the 1950s, and the difference in slopes before and after 1950 was statistically significant at most sites (Supplementary Fig. S2). Although the timing and magnitude of the increase vary among sites, these records indicated a broadly coherent regional increase in soot deposition during the second half of the 20th century.

Source analyses from the SHLW and HGY sediment records provided further insight into this transition. In these two lakes, radiocarbon (^{14}C) analysis was performed on soot samples to distinguish between soot derived from fossil fuels (FF-Soot) and soot derived from biomass burning (BB-Soot)[26,27] (Supplementary Fig. S3). Both the SHLW and HGY records showed that $F^{14}C$ fractions declined while FF-Soot proportions increased beginning around the mid-20th century. During the pre-industrial period from 1900 to 1950, the FF-Soot deposition fluxes were limited, with the proportions generally below 20% (Fig. 3). This indicated that regional emissions during this period were predominantly influenced by biomass burning. After 1950, concurrent with the rapid acceleration of industrialization in China and the sharp increase in coal consumption, the deposition fluxes of FF-Soot in the two lakes increased. In HGY, this proportion gradually rose from 10-20% before 1950 to 40-60% after the 1980s. In SHLW, the proportion of FF-Soot also increased gradually, exceeding 50% after the 1980s. These trends collectively reflected the mid-20th-century transition of China's energy structure from biomass to fossil fuels.

Notably, the timing and magnitude of the increase in soot deposition flux after 1950 varied among different lakes, which may reflect differences in source region influence, atmospheric transport pathways, and sedimentary environments. In addition, compared to SHLW and HGY, other lakes (GH, YJ, CH, TH, QH, Nam Co) are open-basin systems and may be influenced by riverine inputs and outputs. Nevertheless, the soot sediment records of these lakes still show non-significant or weak trends before 1950 and a consistent increasing trend after 1950. This suggests that despite environmental differences among lakes, the low soot flux levels before 1950 reflect China's pre-industrial atmospheric background, while the rapid increase after 1950 identifies human activities as the dominant driver of BC emissions. Although the pace of industrial development varied across different regions of China, industrialization is generally considered to have accelerated during the 1950s.

A comparison with BC ice core records from the Northern Hemisphere revealed pronounced regional heterogeneity in the temporal variability[60,61]. Greenland ice cores generally showed an initial increasing trend followed by decreasing levels since the 1850s, which was mainly influenced by emissions associated with coal combustion in North America and Europe[23,62]. In contrast, several European ice core records exhibited peak BC concentrations around the mid-20th century, corresponding to intensified regional industrial activity[35,63]. Ice cores from the Tibetan Plateau, however, commonly showed increasing BC concentrations beginning around the 1950s, which has been

linked to the rapid growth of anthropogenic emissions in Asia and long-range transport from South and Central Asia[64–67]. This temporal evolution is broadly consistent with soot deposition records reconstructed from lake sediments in this study. While the timing and magnitude of this increase differ across sites, these records collectively reflect the impact of rising regional anthropogenic BC emissions.

Underestimation of early 20th-century BC emissions inferred from sediment records

We used the CESM2 to simulate BC deposition fluxes from 1900 to 2022. Both CESM2 simulations and lake sediment records showed broadly consistent temporal variations in BC deposition across China and captured the transition from biomass burning to fossil fuel dominance since the early 20th century (Figs. 2-3, Supplementary Table S1). However, discrepancies existed before 1950. The ratios between soot fluxes in sediment records and model-simulated BC deposition fluxes in most lakes were generally above 5 before 1950 but decreased afterward. For example, the average ratio in SHLW Lake decreased from 5.96 to 2.70 (Fig. 2 and Supplementary Table S1). Additionally, sediment records showed that biomass burning accounted for approximately 80-90% of total sources, while fossil fuels contributed 10-20%. In contrast, CESM2 simulations showed a lower proportion of fossil fuel sources (approximately 5-10%) (Fig. 3).

In addition to long-term sediment records, modern observational datasets provided further evidence for the model's underestimation of BC concentrations. Results from atmospheric observation sampling conducted at the Qinghai and Beiluhe sites between 2018 and 2019 showed that the simulated values from CESM2 underestimated the surface BC concentrations at both locations, with the ratio of model-simulated to observed values often below 0.5 (Supplementary Fig. S4)[68]. Furthermore, remote sensing datasets verified this underestimation across broader spatial scales. Over multiple years (2000, 2010, 2015, 2022), CESM2 consistently produced simulated values lower than remote sensing data in low-concentration regions, particularly in the northwestern part of China (Supplementary Fig. S5) [69–71]. Evidence from lake sediment records, atmospheric observations, and satellite-retrieved remote sensing datasets consistently indicated that the CESM2 model simulations underestimated atmospheric BC levels over China.

The uncertainties inherent in lake sediment records were smaller than the bias between model simulations and sediment records. Based on propagated uncertainties from component concentration measurements, sediment chronology, and carbon isotope source apportionment (Supplementary Note 1), the relative uncertainties of reconstructed BC, char, and soot fluxes ranged from approximately 17% to 32%, while those of FF-soot and BB-soot fluxes ranged from 22% to 39%. These uncertainty ranges were far smaller than the several-fold differences between CESM2 simulations and lake records, indicating that errors in sediment reconstruction alone cannot account for the observed discrepancy.

In addition, the bias may arise from uncertainties in emission inventories or deficiencies in the representation of physical processes within the model. To verify these possibilities, we conducted a series of sensitivity experiments (Supplementary Note 2 and Supplementary Table S2). Results from the sensitivity experiments showed that perturbations to simulation processes produced relatively modest changes in BC deposition across China, and their impacts remained much smaller than the more than twofold discrepancy indicated by sediment records (Supplementary Fig. S6a-h). In contrast, the emission perturbation experiment (Sens_BC5), which enhances historical background BC emissions, resulted in an increase in simulated BC deposition, bringing model results closer to the

sediment records (Supplementary Fig. S6i). Early emission estimates rely heavily on extrapolated fuel consumption statistics and fixed emission factors, especially for residential combustion and biomass burning sectors, which are known to be highly uncertain[13,14,72]. Previous studies similarly showed that CESM2 simulations using CMIP6 inventories failed to reproduce early 20th-century BC increases recorded in Arctic and Greenland ice cores[15,61,73,74]. Therefore, biases in historical emission inventories were likely the dominant cause of the inconsistency between model simulations and sediment records.

Modeled climate responses to adjusted historical BC emissions

To assess the climatic effects of the historical underestimation of BC emissions, we designed the Base experiment (benchmark emission scenario) and the Sens_BC5 experiment (enhanced emission scenario). Compared with the Base experiment, the Sens_BC5 experiment improved the spatiotemporal consistency between the BC fluxes simulated by the CESM2 model and the soot fluxes in lake sediment records. In the SHLW sediment record, the average ratio of soot flux to simulated BC flux decreased from 5.96 to 2.65 before 1950, and from 2.75 to 1.86 after 1950 (Supplementary Fig. S7). Both the Base and Sens_BC5 experiments captured the transition in BC emission sources from biomass burning to fossil fuel combustion dominance, consistent with sediment record observations. While the Sens_BC5 experiment moderately increased fossil fuel emissions, resulting in an increase in the total BC deposition flux, the relative contribution of each emission source showed only marginal changes (Supplementary Fig. S8).

In addition, the Sens_BC5 experiment better replicated the atmospheric BC concentrations observed at Qinghai and Beiluhe stations during 2018-2019, with the ratio of simulated to observed values being close to 1 (Supplementary Fig. S4). Further comparisons with remote sensing datasets (Supplementary Fig. S5) indicated that the increase in emissions mainly raised BC concentrations in western and eastern China, improving consistency between model results and satellite-derived BC data.

Compared with the Base experiment, the Sens_BC5 experiment produced stronger radiative and temperature responses, particularly in high-latitude regions. Globally, the enhanced emissions increased the mean surface temperature by 0.03 K and the net solar flux at the top of the atmosphere (FSNTOA) by 0.30 W m^{-2} (Fig. 4a-d). However, the response exhibited strong regional heterogeneity rather than a spatially uniform pattern. The Arctic (north of 60°N) showed the most pronounced response, with a temperature increase of 0.13 K and an increase in FSNTOA of 1.05 W m^{-2}, exceeding responses in mid-latitudes (30°N-60°N: ΔT = +0.04 K, ΔFSNTOA = +0.52 W m^{-2}) and minimal responses in the equatorial and Southern Hemisphere (Fig. 4a-d).

Radiative and temperature responses also displayed pronounced seasonal variability. During spring and summer, the FSNTOA north of 60°N increased by approximately 1.90 W m^{-2} and 2.10 W m^{-2}, respectively, accompanied by surface warming of about 0.20 K (Fig. 5). At the regional scale, these seasonal anomalies were particularly pronounced over northern Siberia and parts of North America, where increases in FSNTOA exceeded 10.0 W m^{-2} and surface warming approached 1.50 K (Fig. 5).

BC deposition on snow decreases snow albedo and increases solar radiation absorption, leading to a warming response[7,11,21]. This warming can further affect snow microphysical properties, sublimation rates, and melt processes, potentially exacerbating the reductions in snowpack albedo induced by BC and amplifying the associated radiative forcing[1]. However, regions with enhanced BC deposition in snow did not exhibit a simple linear relationship with the

magnitude of warming. Although relatively high BC mass concentrations in snow were simulated in parts of northern Russia, the resulting acceleration of snowmelt and the associated surface temperature responses exhibited spatial variability (Fig. 4 and Supplementary Fig. S9). These findings indicated that BC-snow interactions were influenced not only by BC concentrations within the snowpack but also by prevailing environmental conditions, including snow physical properties, solar radiation, cloud cover, and surface energy balance.

Seasonal analysis further illustrated the influence of solar radiation on Arctic climate responses. In spring and summer, temperature anomalies north of 60°N demonstrated significant spatial correlations with radiative fluxes (ΔFSNTOA and ΔFSNS), with correlation coefficients exceeding 0.7 (Fig. 5 and Supplementary Fig. S10). In contrast, during winter, these correlations were weak. Snow cover fraction provided further context for understanding seasonal variability (Supplementary Fig. S11). In spring, extensive snow cover (greater than 90%) coincided with increasing solar radiation, which enhanced shortwave absorption due to reduced surface reflectivity. The most significant decline in snow cover fraction occurred in summer (approximately 4%), reflecting accelerated snow retreat and intensified surface darkening feedbacks. This effect gradually diminished in autumn and winter. By winter, snow cover reached 99%, and differences between the two experiments became negligible. The snow-albedo feedback in the Northern Hemisphere reaches its peak when the combined effects of snow cover and insolation are most pronounced, particularly when snow is at or near the melting threshold[1]. Consequently, this feedback is most evident in spring and summer, when extensive snow cover coincides with heightened solar radiation. Under these conditions, even slight reductions in surface reflectivity can significantly increase solar radiation absorption and lead to marked surface warming. In contrast, solar radiation decreases significantly in autumn and winter. Although BC remains within the snowpack, the reduced shortwave energy input diminishes the radiative forcing associated with snow darkening.

By contrast, the updated emissions had a limited effect on global precipitation, with only minor decreases observed in some mid-to-low-latitude regions and no significant global or regional patterns detected (Fig. 4e and Fig. 4f). The weak hydrological response was consistent with earlier studies, which found only minor precipitation increases even under full removal of anthropogenic BC emissions[19,20].

Previous research examining the Arctic climate response to BC often relied on idealized scenarios involving artificially scaled emissions or concentration-driven perturbations[10–12,21]. This study applied observationally constrained corrections derived from sediment records, providing a more realistic reconstruction of historical BC emissions. This approach represented an important step toward integrating geological archives with climate modeling to better assess historical aerosol forcing.

Uncertainties and limitations

Although the simulations using enhanced historical BC emissions showed improved consistency with observations, several sources of uncertainty remained in this study.

Uncertainty existed in both the reconstruction of historical BC emissions and the spatial representativeness of lake sediment records. Historical emission inventories were limited by incomplete activity data and simplified assumptions regarding fuel use, combustion technology, and population dynamics. In this study, we conducted a simplified revision of biomass burning BC emissions before 1950 based on population data. However, uncertainty remained in the spatial distribution of these emissions across regions with varying fuel consumption practices. While

lake sediment records provided long-term archives of atmospheric BC deposition, their representativeness depended on local catchment characteristics, atmospheric transport pathways, and regional emission sources. Even in closed systems (maar lakes), the actual spatial extent captured by sediment records remained to be further quantified. Consequently, applying constraints from a limited number of sediment records to improve large-scale emission inventories inevitably introduced additional uncertainty.

Additional uncertainty arose from the representation of atmospheric BC processes in climate models. Processes including aerosol aging, convective transport, and in-cloud wet scavenging influenced BC atmospheric lifetime and deposition efficiency. Sensitivity experiments conducted with CESM2 indicated that variations in these processes altered simulated BC deposition at lake sites by approximately ±20%, with a maximum change of about 38% at Nam Co (Supplementary Fig. S6). These results showed the sensitivity of BC deposition to aerosol process parameterizations and indicated the importance of accurately representing these processes in climate models.

Finally, uncertainty inherent in BC deposition fluxes estimated from lake sediments must be considered. Flux calculations were influenced by analytical measurement uncertainty, chronological uncertainty associated with sediment dating, and uncertainty in source apportionment between fossil fuel and biomass sources based on radiocarbon analysis (Supplementary Note 1). Error propagation analysis suggested that the relative uncertainties of BC, char, and soot fluxes ranged from approximately 17% to 32%, while those of FF-soot and BB-soot fluxes ranged from about 22% to 39%, depending mainly on the chronology method applied. Although these uncertainties did not affect the overall temporal trends observed in sediment records, they contributed to the uncertainty range of reconstructed BC deposition fluxes. Sedimentary processes may also influence the recorded fluxes. In addition to atmospheric deposition, BC preserved in lake sediments can be affected by catchment transport and sediment redistribution. For instance, flood or storm events may mobilize residual BC from the watershed and transport it to the lake, resulting in peaks that are not directly correlated with atmospheric deposition[75]. Even in closed-basin lakes, the sediment focusing effect associated with lateral sediment transport from littoral zones to the lake center can still impact the sediment accumulation rates and fluxes in sediment cores[76]. To reduce these potential influences, this study focused on closed-basin lakes where atmospheric deposition was the primary input pathway (SHLW and HGY) and compiled multiple representative lake records across China. Nevertheless, some uncertainties related to sediment transport and focusing processes still remained.

Future studies should integrate multiple observational archives, including ice cores, lake sediments, and isotopic tracers, to better constrain early BC emission histories. Additionally, multi-model intercomparisons are crucial for quantifying uncertainty related to aerosol processes, transport pathways, and emission inventories. These efforts will help refine estimates of historical BC forcing, improve the attribution of observed Arctic climate change, and provide scientific support for mitigation strategies using BC reduction as an effective short-term climate intervention.

Methods

Soot measurement and flux calculation in lake sediment records

Figure 1a illustrates the geographical distribution of the studied lake sites and the annual average BC emissions from 1850 to 2019. QH and Nam Co are located on the Tibetan Plateau, where local BC emissions are minimal due

to limited human activity. BC deposition at these sites is primarily influenced by long-range atmospheric transport rather than local sources. GH, located in north-central China, experiences a moderate anthropogenic influence. Lakes CH, TH (eastern China), and YJ (central China) have been significantly impacted by industrial expansion, resulting in heightened anthropogenic BC deposition over time. CH, Nam Co, QH, GH, TH, and YJ are open-basin lakes, implying potential hydrological influences (river inflows and outflows) on their BC deposition records. In contrast, Lake HGY, a volcanic crater lake in southeastern China, lacks fluvial connections due to its steep lava walls, ensuring BC deposition is primarily atmospheric. However, nearby industrial activities likely enhance BC inputs. Similarly, Lake SHLW, a closed-basin volcanic lake in northeastern China's Jingyu County, exhibits negligible direct human influence, with atmospheric deposition as its sole BC source, making it ideal for studying background emissions. All lake characteristics and detailed information are listed in Supplementary Table S1 and Supplementary Table S3.

In this study, the TOR method was applied to SHLW sediment core samples to quantify the concentrations of BC, char, and soot, with sampling details described in Han et al.[27]. Following the IMPROVE_A protocol, four organic carbon fractions (OC1-OC4 from 150, 280, 480 to 580 °C) were produced in a pure helium atmosphere, while three elemental carbon fractions (EC1-EC3 from 580, 730 to 830°C) were produced in a 2% O_2/98% He atmosphere and the pyrolysis of organic carbon (defined as POC) took place in a pure helium atmosphere. The protocol calculated BC as EC1 + EC2 + EC3 – POC, char as EC1– POC, and soot as EC2 + EC3[42]. Additional methodological details are provided in prior work[32]. The deposition fluxes of BC, char, and soot in the sediment cores were calculated using the following equation:

$$Flux_{(BC,Char,Soot)} = MAR \times C_{(BC,Char,Soot)} \quad (1)$$

Where $Flux_{(BC,Char,Soot)}$ is the deposition flux, MAR is the mass accumulation rate, and $C_{(BC,Char,Soot)}$ is the measured concentration. Detailed information on MAR is provided in Han et al.[27].

Radiocarbon (^{14}C) analysis was further conducted on soot samples to distinguish between FF-Soot and BB-Soot. Briefly, sediment samples were pretreated with acid to remove carbonate, minerals and oxides, and then filtered using pre-fired quartz filters. The soot fraction was then isolated using a three-step combustion protocol[77] and converted to CO_2 using an Automated Aerosol Combustion (AAC) system[78]. The CO_2 collected during the combustion of soot was subjected to ^{14}C analysis[79]. The measured $F^{14}C$ values were corrected for instrument background, memory effects, and procedural contamination, and were normalized using standard reference materials. The fossil fuel fraction was calculated from the measured $F^{14}C$ values. In this calculation, we assumed that biomass soot in the SHLW mainly originated from the burning of 50% 50-year-old trees and 50% crops[27]. The uncertainty analysis of each component flux in lake sediments is detailed in Supplementary Note 1.

Model and experimental design

Model description and emissions

CESM2 is a fully coupled Earth system model that incorporates atmospheric chemistry, biogeochemistry, and anthropogenic processes. Its atmospheric component is configured with the Community Atmosphere Model version 6 (CAM6) [80], which includes updated physical parameterizations. All simulations were conducted at a horizontal resolution of 1.9° × 2.5°, covering the period 1850-2022. The first 50 years (1850-1900) were excluded as spin-up. Simulations were performed with prescribed sea surface temperature and sea ice conditions.

Anthropogenic and biomass burning emissions were derived from the CMIP7 input4MIPs datasets. Historical anthropogenic emissions are based on an updated version of the Community Emissions Data System (CEDS)[72], which improves national-level emission trend estimates for China, Europe, and North America, and enhances consistency with subnational statistics and regional inventories. Notably, the CMIP7 inventory captures the post-2010 emission peak and subsequent decline in China. Open biomass burning emissions were taken from the BB4CMIP dataset[81]. The dataset integrates satellite observations, fire modeling, and historical proxies, and its latest version provides global fire emission data from 1750 to 2022. Other emissions used in CESM2 are described in Emmons et al.[82]. Emission sources in this study were categorized into three types: Fossil Fuel Combustion (FF), Anthropogenic Biomass Burning (anthro-BB), and Open Biomass Burning (open-BB).

Emission enhancement experiment

To assess the potential climatic impacts of underestimated BC emissions during historical periods, this study designed two sets of simulation experiments: the Base experiment, which uses unmodified CMIP7 emissions, and the Sens_BC5 experiment, which incorporates enhanced historical BC emissions.

The magnitude of emission enhancement was constrained by an independent reconstruction of biomass burning BC emissions in China. This reconstruction relies on a newly developed regional biomass burning emission inventory for China covering the period 1980-2022 (https://www.lsdc.ac.cn/portal/data/2621)[83]. Based on the BC emission data from this inventory for the years 1980 to 2003, historical emissions prior to 1980 were reconstructed and extended back to 1900 using population data (see Supplementary Note 3 for details). The reconstruction showed that biomass burning BC emissions in China before 1950 were higher than the estimates provided by the CMIP7 inventory, which lies near the lower bound of the 90% confidence interval of the reconstructed results (Supplementary Fig. S12). Constrained by this independent reconstruction, this study adopted a fivefold enhancement factor, corresponding to the central tendency of the reconstructed uncertainty range (Supplementary Fig. S13).

In Sens_BC5, we first calculated the average BC emissions from biomass burning during 1850-1950 across Asia, then scaled this average by a factor of five and uniformly added it to all Asian grid cells. The enhanced emissions were calculated as:

$$E'_{i,j} = E_{i,j} + 5 \times E^{Asia}_{1850-1950} \quad (2)$$

Where $E_{i,j}$ represents the original BC emissions at grid cell (i, j), and $E^{Asia}_{1850-1950}$ represents the average BC emissions from biomass burning in the Asian region during 1850-1950. In this study, we adopted an additive approach with a constant enhancement magnitude to reflect the systematic underestimation of background BC emissions in historical emission inventories, rather than a proportional bias or annual variability applicable to all periods. Considering the substantial uncertainties and limited observational constraints prior to 1950, this fixed correction factor avoided overfitting and provides a conservative estimate of the potential underestimation in historical emissions. Due to significant spatial heterogeneity in emissions across China, the total BC emissions increased by approximately 1.5 to 2 times in China after the adjustment (Supplementary Fig. S13).

In addition, modest adjustments to source fractions were made. Results from lake sediment records show that before 1950, soot deposition flux in China was mainly derived from biomass burning, accounting for 80%-90%, while the contribution of fossil fuels was approximately 10%-20%[26,84]. In contrast, the CMIP7 input4MIPs dataset estimates that the contribution of fossil fuels during the same period was only 5%-10%. To better reflect historical source

structure, we increased fossil fuel BC emissions in the pre-1950 period to maintain their contribution at approximately 10% (Supplementary Fig. S13).

Data availability

The CESM2 model is publicly available from the National Center for Atmospheric Research and is publicly available at https://www.cesm.ucar.edu/. Anthropogenic emissions were obtained from the CMIP7 input4MIPs dataset based on the Community Emissions Data System (CEDS), and open biomass burning emissions were from the BB4CMIP dataset. Both datasets are publicly available via the Earth System Grid Federation (ESGF) portal (https://esgf-node.llnl.gov/). The reconstructed biomass burning BC emission dataset used in this study is available at the National Tibetan Plateau Data Center (https://www.lsdc.ac.cn/portal/data/2621). The Tracking China Air Pollution (TAP) dataset used in this study is available at http://tapdata.org.cn. The original datasets used for figure generation and analysis in this study are publicly available from Zenodo at https://zenodo.org/records/20092189. Sediment records for additional lakes used in this study were previously published and are available in the cited literature[26,54–59].

References

1. Bond, T. C. *et al.* Bounding the role of black carbon in the climate system: A scientific assessment. *J. Geophys. Res. Atmos.* **118**, 5380–5552 (2013).
2. Corbin, J. C. *et al.* Infrared-absorbing carbonaceous tar can dominate light absorption by marine-engine exhaust. *npj Clim. Atmos. Sci.* **2**, 12 (2019).
3. Jacobson, M. Z. Strong radiative heating due to the mixing state of black carbon in atmospheric aerosols. *Nature* **409**, 695–697 (2001).
4. Anenberg, S. C. *et al.* Impacts of global, regional, and sectoral black carbon emission reductions on surface air quality and human mortality. *Atmos. Chem. Phys.* **11**, 7253–7267 (2011).
5. Zhao, G. *et al.* Mixing state of black carbon at different atmospheres in north and southwest China. *Atmos. Chem. Phys.* **22**, 10861–10873 (2022).
6. Andreae, M. O. & Ramanathan, V. Climate's Dark Forcings. *Science* **340**, 280–281 (2013).
7. Flanner, M. G., Zender, C. S., Randerson, J. T. & Rasch, P. J. Present-day climate forcing and response from black carbon in snow. *J. Geophys. Res. Atmos.* **112**, 2006JD008003 (2007).
8. Qian, Y., Wang, H., Zhang, R., Flanner, M. G. & Rasch, P. J. A sensitivity study on modeling black carbon in snow and its radiative forcing over the Arctic and Northern China. *Environ. Res. Lett.* **9**, 064001 (2014).
9. Hansen, J. & Nazarenko, L. Soot climate forcing via snow and ice albedos. *Proc. Natl. Acad. Sci. U.S.A.* **101**, 423–428 (2004).
10. Flanner, M. G. Arctic climate sensitivity to local black carbon. *J. Geophys. Res. Atmos.* **118**, 1840–1851 (2013).
11. Sand, M., Berntsen, T. K., Seland, Ø. & Kristjánsson, J. E. Arctic surface temperature change to emissions of black carbon within Arctic or midlatitudes. *J. Geophys. Res. Atmos.* **118**, 7788–7798 (2013).
12. Shindell, D. & Faluvegi, G. Climate response to regional radiative forcing during the twentieth century. *Nat. Geosci.* **2**, 294–300 (2009).
13. Bond, T. C. *et al.* Historical emissions of black and organic carbon aerosol from energy-related combustion, 1850–2000. *Glob. Biogeochem. Cycles* **21**, 2006GB002840 (2007).
14. Novakov, T. *et al.* Large historical changes of fossil-fuel black carbon aerosols. *Geophys. Res. Lett.* **30**, 2002GL016345 (2003).

15. Eckhardt, S. *et al.* Revised historical Northern Hemisphere black carbon emissions based on inverse modeling of ice core records. *Nat. Commun.* **14**, 271 (2023).
16. Zhang, B. *et al.* Improved biomass burning emissions from 1750 to 2010 using ice core records and inverse modeling. *Nat. Commun.* **15**, 3651 (2024).
17. Stjern, C. W. *et al*. Rapid Adjustments Cause Weak Surface Temperature Response to Increased Black Carbon Concentrations. *J. Geophys. Res. Atmos.* **122**, 462–481 (2017).
18. Yang, Y., Smith, S. J., Wang, H., Mills, C. M. & Rasch, P. J. Variability, timescales, and nonlinearity in climate responses to black carbon emissions. *Atmos. Chem. Phys.* **19**, 2405–2420 (2019).
19. Baker, L. H. *et al.* Climate responses to anthropogenic emissions of short-lived climate pollutants. *Atmos. Chem. Phys.* **15**, 8201–8216 (2015).
20. Andrews, T., Forster, P. M., Boucher, O., Bellouin, N. & Jones, A. Precipitation, radiative forcing and global temperature change. *Geophys. Res. Lett.* **37**, 2010GL043991 (2010).
21. Sand, M. *et al.* Response of Arctic temperature to changes in emissions of short-lived climate forcers. *Nat. Clim. Change* **6**, 286–289 (2016).
22. Legrand, M. *et al.* Cadmium Pollution From Zinc-Smelters up to Fourfold Higher Than Expected in Western Europe in the 1980s as Revealed by Alpine Ice. *Geophys. Res. Lett.* **47**, 2020GL087537 (2020).
23. McConnell, J. R. *et al.* 20th-Century Industrial Black Carbon Emissions Altered Arctic Climate Forcing. *Science* **317**, 1381–1384 (2007).
24. Ming, J. *et al.* Black carbon record based on a shallow Himalayan ice core and its climatic implications. *Atmos. Chem. Phys.* **8**, 1343–1352 (2008).
25. Xu, B. *et al.* Black soot and the survival of Tibetan glaciers. *Proc. Natl. Acad. Sci. U.S.A.* **106**, 22114–22118 (2009).
26. Han, Y. *et al.* Sediment Soot Radiocarbon Indicates that Recent Pollution Controls Slowed Fossil Fuel Emissions in Southeastern China. *Environ. Sci. Technol.* **56**, 1534–1543 (2022).
27. Han, Y. *et al.* The Sihailongwan Maar Lake, northeastern China as a candidate Global boundary Stratotype Section and Point for the Anthropocene series. *Anthropocene Rev.* **10**, 177–200 (2023).
28. Goldberg, S. & Sposito, G. A Chemical Model of Phosphate Adsorption by Soils: I. Reference Oxide Minerals. *Soil Sci. Soc. Am. J.* **48**, 772–778 (1985).
29. Masiello, C. A. New directions in black carbon organic geochemistry. *Marine Chemistry* **92**, 201–213 (2004).

30. Hammes, K. *et al.* Comparison of quantification methods to measure fire-derived (black/elemental) carbon in soils and sediments using reference materials from soil, water, sediment and the atmosphere. *Glob. Biogeochem. Cycles* **21**, 2006GB002914 (2007).

31. Elmquist, M., Cornelissen, G., Kukulska, Z. & Gustafsson, Ö. Distinct oxidative stabilities of char versus soot black carbon: Implications for quantification and environmental recalcitrance. *Glob. Biogeochem. Cycles* **20**, 2005GB002629 (2006).

32. Han, Y. M. *et al.* Comparison of Elemental Carbon in Lake Sediments Measured by Three Different Methods and 150-Year Pollution History in Eastern China. *Environ. Sci. Technol.* **45**, 5287–5293 (2011).

33. Han, Y. M. *et al.* Reconstruction of atmospheric soot history in inland regions from lake sediments over the past 150 years. *Sci. Rep.* **6**, 19151 (2016).

34. Lohmann, U. *et al.* Future warming exacerbated by aged-soot effect on cloud formation. *Nat. Geosci.* **13**, 674–680 (2020).

35. Sigl, M. *et al.* 19th century glacier retreat in the Alps preceded the emergence of industrial black carbon deposition on high-alpine glaciers. *The Cryosphere* **12**, 3311–3331 (2018).

36. Jeong, C.-H. *et al.* Identification of the Sources and Geographic Origins of Black Carbon using Factor Analysis at Paired Rural and Urban sites. *Environ. Sci. Technol.* **47**, 8462–8470 (2013).

37. Ikeda, K. *et al.* Model and Satellite Analysis of Transport of Asian Anthropogenic Pollution to the Arctic: Siberian and Pacific Pathways and Their Meteorological Controls. *J. Geophys. Res. Atmos.* **126**, e2020JD033459 (2021).

38. Ikeda, K. *et al.* Tagged tracer simulations of black carbon in the Arctic: transport, source contributions, and budget. *Atmos. Chem. Phys.* **17**, 10515–10533 (2017).

39. Backman, J., Schmeisser, L. & Asmi, E. Asian Emissions Explain Much of the Arctic Black Carbon Events. *Geophys. Res. Lett.* **48**, e2020GL091913 (2021).

40. He, C. *et al.* Black carbon pollution in China from 2001 to 2019: Patterns, trends, and drivers. *Environ. Pollut.* **324**, 121381 (2023).

41. Wang, R. *et al.* Black Carbon Emissions in China from 1949 to 2050. *Environ. Sci. Technol.* **46**, 7595–7603 (2012).

42. Han, Y. *et al.* Evaluation of the thermal/optical reflectance method for quantification of elemental carbon in sediments. *Chemosphere* **69**, 526–533 (2007).

43. Schmidt, M. W. I. & Noack, A. G. Black carbon in soils and sediments: Analysis, distribution, implications, and current challenges. *Glob. Biogeochem. Cycles* **14**, 777–793 (2000).
44. Cai, J. *et al.* Char dominates black carbon aerosol emission and its historic reduction in China. *Nat. Commun.* **14**, 6444 (2023).
45. Coppola, A. I. *et al.* The black carbon cycle and its role in the Earth system. *Nat. Rev. Earth Environ.* **3**, 516–532 (2022).
46. Ramanathan, V. & Carmichael, G. Global and regional climate changes due to black carbon. *Nat. Geosci.* **1**, 221–227 (2008).
47. Petzold, A. *et al.* Recommendations for reporting 'black carbon' measurements. *Atmos. Chem. Phys.* **13**, 8365–8379 (2013).
48. IPCC. 2019 Refinement to the 2006 IPCC Guidelines for National Greenhouse Gas Inventories. Volume 4: Agriculture, Forestry and Other Land Use, Chs. 2 and 6 (Intergovernmental Panel on Climate Change, 2019).
49. Wu, H., Wang, J., Guo, J., Hu, X. & Chen, J. Sedimentary records of polycyclic aromatic hydrocarbons from three enclosed lakes in China: Response to energy structure and economic development. *Environ. Pollut.* **318**, 120929 (2023).
50. Xu, D. *et al.* Synchronous 500-year oscillations of monsoon climate and human activity in Northeast Asia. *Nat. Commun.* **10**, 4105 (2019).
51. Xu, D. *et al.* Asynchronous 500-year summer monsoon rainfall cycles between Northeast and Central China during the Holocene. *Glob. Planet. Change* **195**, 103324 (2020).
52. Stebich, M. *et al.* Holocene vegetation and climate dynamics of NE China based on the pollen record from Sihailongwan Maar Lake. *Quat. Sci. Rev.* **124**, 275–289 (2015).
53. Gong, X. *et al.* Spatiotemporal patterns and drivers of wildfire CO_2 emissions in China from 2001 to 2022. *Atmos. Chem. Phys.* **25**, 10379–10401 (2025).
54. Han, Y. M. *et al.* Distribution and ecotoxicological significance of trace element contamination in a ~150 yr record of sediments in Lake Chaohu, Eastern China. *J. Environ. Monit.* **13**, 743–752 (2011).
55. Cong, Z. *et al.* Historical Trends of Atmospheric Black Carbon on Tibetan Plateau As Reconstructed from a 150-Year Lake Sediment Record. *Environ. Sci. Technol.* **47**, 2579–2586 (2013).

56. Han, Y. M. *et al.* Elemental Carbon and Polycyclic Aromatic Compounds in a 150-Year Sediment Core from Lake Qinghai, Tibetan Plateau, China: Influence of Regional and Local Sources and Transport Pathways. *Environ. Sci. Technol.* **49**, 4176–4183 (2015).
57. Zhan, C., Wan, D., Han, Y. & Zhang, J. Historical variation of black carbon and PAHs over the last ~200 years in central North China: Evidence from lake sediment records. *Sci. Total Environ.* **690**, 891–899 (2019).
58. Zhan, C. *et al.* Decadal trends of black carbon and heavy metal accumulation in a lake sediment core from central China: A historical perspective. *Catena* **247**, 108513 (2024).
59. Han, Y., Cao, J., Jin, Z., Liu, S. & An, Z. Comparative study of char and soot in sediments from Daihai and Taihu lakes over the past 200 years. *Quat. Sci.* 30, 550–558 (2010) (in Chinese).
60. Kang, S., Zhang, Y., Qian, Y. & Wang, H. A review of black carbon in snow and ice and its impact on the cryosphere. *Earth-Sci. Rev.* **210**, 103346 (2020).
61. Chen, Y. *et al.* A Comprehensive Evaluation of Black Carbon in Snow and Its Radiative Forcing in CMIP5 and CMIP6 Models Based on Global Field Observations. *J. Geophys. Res. Atmos.* **129**, e2023JD040665 (2024).
62. Koch, D. *et al.* Coupled Aerosol-Chemistry–Climate Twentieth-Century Transient Model Investigation: Trends in Short-Lived Species and Climate Responses. *J. Clim.* **24**, 2693–2714 (2011).
63. Lim, S. *et al.* Black carbon variability since preindustrial times in the eastern part of Europe reconstructed from Mt. Elbrus, Caucasus, ice cores. *Atmos. Chem. Phys.* **17**, 3489–3505 (2017).
64. Wang, M. *et al.* Black carbon deposited in Hariqin Glacier of the Central Tibetan Plateau record changes in the emission from Eurasia. *Environ. Pollut.* **273**, 115778 (2021).
65. Wang, M. *et al.* Century-long record of black carbon in an ice core from the Eastern Pamirs: Estimated contributions from biomass burning. *Atmos. Environ.* **115**, 79–88 (2015).
66. Kaspari, S. D. *et al.* Recent increase in black carbon concentrations from a Mt. Everest ice core spanning 1860-2000 AD. *Geophys. Res. Lett.* **38**, L04703 (2011).
67. Jenkins, M., Kaspari, S., Kang, S.-C., Grigholm, B. & Mayewski, P. A. Tibetan Plateau Geladaindong black carbon ice core record (1843–1982): Recent increases due to higher emissions and lower snow accumulation. *Adv. Clim. Change Res.* **7**, 132–138 (2016).
68. Zhu, C. *et al.* Black Carbon and Secondary Brown Carbon, the Dominant Light Absorption and Direct Radiative Forcing Contributors of the Atmospheric Aerosols Over the Tibetan Plateau. *Geophys. Res. Lett.* **48**, e2021GL092524 (2021).

69. Liu, S. *et al.* Tracking Daily Concentrations of $PM_{2.5}$ Chemical Composition in China since 2000. *Environ. Sci. Technol.* **56**, 16517–16527 (2022).

70. Geng, G. *et al.* Chemical composition of ambient $PM_{2.5}$ over China and relationship to precursor emissions during 2005–2012. *Atmos. Chem. Phys.* **17**, 9187–9203 (2017).

71. Tracking China Air Pollution (TAP)[Dataset]. http://tapdata.org.cn (accessed April 2026).

72. Hoesly, R. M. *et al.* Historical (1750–2014) anthropogenic emissions of reactive gases and aerosols from the Community Emissions Data System (CEDS). *Geosci. Model Dev.* **11**, 369–408 (2018).

73. Bauer, S. E. *et al.* Historical and future black carbon deposition on the three ice caps: Ice core measurements and model simulations from 1850 to 2100. *J. Geophys. Res. Atmos.* **118**, 7948–7961 (2013).

74. Moseid, K. O. *et al.* Using Ice Cores to Evaluate CMIP6 Aerosol Concentrations Over the Historical Era. *J. Geophys. Res. Atmos.* **127**, e2021JD036105 (2022).

75. Smith, D. M., Griffin, J. J. & Goldberg, E. D. Spectrometric method for the quantitative determination of elemental carbon. *Anal. Chem.* **47**, 233–238 (1975).

76. Baskaran, M., Nix, J., Kuyper, C. & Karunakara, N. Problems with the dating of sediment core using excess ^{210}Pb in a freshwater system impacted by large scale watershed changes. *J. Environ. Radioact.* **138**, 355–363 (2014).

77. Dusek, U. *et al.* Evaluation of a two-step thermal method for separating organic and elemental carbon for radiocarbon analysis. *Atmos. Meas. Tech.* **7**, 1943–1955 (2014).

78. Dusek, U. *et al.* Technical Note: An Automated System for Separate Combustion of Elemental and Organic Carbon for ^{14}C Analysis of Carbonaceous Aerosol. *Aerosol Air Qual. Res.* **19**, 2604–2611 (2019).

79. Ruff, M. *et al.* A Gas Ion Source for Radiocarbon Measurements at 200 kV. *Radiocarbon* **49**, 307–314 (2007).

80. Wu, C., Liu, X., Lin, Z., Rahimi-Esfarjani, S. R. & Lu, Z. Impacts of absorbing aerosol deposition on snowpack and hydrologic cycle in the Rocky Mountain region based on variable-resolution CESM (VR-CESM) simulations. *Atmos. Chem. Phys.* **18**, 511–533 (2018).

81. van Marle, M. J. E. *et al.* Historic global biomass burning emissions for CMIP6 (BB4CMIP) based on merging satellite observations with proxies and fire models (1750–2015). *Geosci. Model Dev.* **10**, 3329–3357 (2017).

82. Emmons, L. K. *et al.* The Chemistry Mechanism in the Community Earth System Model Version 2 (CESM2). *J. Adv. Model. Earth Syst.* **12**, e2019MS001882 (2020).

83. HAN, Y. & Gong, X. China Regional Biomass Combustion Emission Dataset (1980-2024) [Data set]. Loess Science Data Center, Institute of Earth Environment, Chinese Academy of Sciences. https://doi.org/10.12262/lsdc.17015.2621 (accessed April 2026).

84. Tang, Y. *et al*. Tracing sources of sedimentary soot: The underestimated role of liquid fossil fuels in North China. *J. Hazard. Mater.* **493**, 138408 (2025).

Author contributions

Xuehong Gong conceived and designed the study, compiled the sediment datasets, performed data analysis, conducted model simulations, and wrote the original draft. Yongming Han conceived and designed the study, supervised the research, and contributed to manuscript revision. Chongshu Zhu contributed to sediment data compilation and participated in data analysis. Tzung-May Fu contributed to model configuration and supported the interpretation of simulation results. Qiyuan Wang assisted in sediment data processing and contributed to data analysis. Dewen Lei supported sediment data collection and assisted in data analysis. Jiaoyang Yu contributed to model setup and the interpretation of simulation results. Ruonan Wang contributed to model implementation and assisted in interpreting the simulation outputs. Zhisheng An contributed to the scientific interpretation and discussion of the results. Guohui Li conceived and designed the study, supervised the research, and revised the manuscript. All authors contributed to the discussion of the results and approved the final version of the manuscript.

Funding

This work was supported by the National Natural Science Foundation of China (grant nos. 42221003).

Competing interests

The authors declare no competing interests.

Fig. 1: Characteristics of soot fluxes in Sihailongwan Maar Lake (SHLW) based on sediment records and regional BC emissions.

Figure (**a**) shows the spatial distribution of the average BC emissions (anthropogenic and biomass burning, in g m^{-2} yr^{-1}) from 1850 to 2022. SHLW (red star) and other research lakes analyzed in this study (blue dots) are marked. The studied lakes include Sihailongwan Maar Lake (SHLW) (this study), Huguangyan Lake (HGY) (ref. 26), Chaohu Lake (CH) (ref. 54), Nam Co (ref. 55), Qinghai Lake (QH) (ref. 56), Gonghai Lake (GH) (ref. 57), Yinjia Lake (YJ) (ref. 58), and Taihu Lake (TH) (ref. 59). The blue bars above each lake represent the annual average soot flux based on sediment records. Figure (**b**) is a photograph of SHLW and its surrounding environment. Photograph courtesy of Mr. Pengfei Ji at Jilin TV Station (ref. 27). Figure (**c**) shows the temporal trend of soot flux in SHLW Lake from 1900 to 2019. The blue line represents the raw data, the yellow line represents the 5-year smoothed trend, and the red dashed line represents the linear trend. Figure (**d**) presents the frequency distribution of soot flux, where the red dashed line indicates the average value, highlighting the distribution characteristics of soot flux in SHLW during the study period. Base map data in Figure (**a**) were adapted from Tianditu (National Platform for Common Geospatial Information Services, China, https://www.tianditu.gov.cn/) and from OpenStreetMap contributors (CC BY-SA). Basemap imagery was hosted by Esri ArcGIS Online. Maps were created using ArcGIS® software by Esri. All other elements are original to this work.

Fig. 2: Comparison of deposition fluxes between lake sediment records and CESM simulations across Chinese lakes.

Figures correspond to (**b**) Sihailongwan Maar Lake (SHLW) (this study), (**c**) Huguangyan Lake (HGY) (ref. 26), (**d**) Chaohu Lake (CH) (ref. 54), (**e**) Nam Co (ref. 55), (**f**) Qinghai Lake (QH) (ref. 56), (**g**) Gonghai Lake (GH) (ref. 57), (**h**) Yinjia Lake (YJ) (ref. 58), and (**i**) Taihu Lake (TH) (ref. 59). (**a**) Distribution of the ratio between soot deposition fluxes in lake sediments and BC deposition fluxes simulated by the Base experiment using the CESM2 model at the corresponding grid cells. Orange indicates values before 1950 (left) and red indicates values after 1950 (right). The violin shapes show the probability density of annual ratios, while the embedded boxplots represent the median, interquartile range, and whiskers. Ratios greater than one indicate that the model underestimates BC deposition relative to sediment records. (**b–i**) Time series comparison of soot fluxes from lake sediment records (red crosses, left axis) and modeled BC deposition fluxes from the Base experiment using the CESM2 model (blue lines, right axis). The grey shading indicates the period prior to 1950.

Fig. 3: Comparison of fossil fuel and biomass burning contributions to deposition fluxes between lake sediment records and CESM simulations.

Figures **(a-d)** show comparisons for Sihailongwan Maar Lake (SHLW), and Figures **(e-h)** for Huguangyan Lake (HGY). **(a, e)** Temporal variations in BC fluxes derived from fossil fuels (FF-BC flux) simulated by CESM2 model (green; right axis; dashed lines) and soot fluxes derived from fossil fuels (FF-Soot flux) in lake sediment records (blue; left axis; solid lines). (**b, f**) Temporal variations in BC fluxes derived from biomass burning (BB-BC flux) simulated by CESM2 model (red; right axis; dashed lines) and soot fluxes derived from biomass burning (BB-Soot flux) in lake sediment records (orange; left axis; solid lines). **(c, g)** Fractional contribution of fossil fuel sources to total BC deposition in CESM2 simulations (dashed lines) and to total soot flux in lake

sediments (solid lines). **(d, h)** Fractional contribution of biomass burning sources to total BC deposition in CESM2 simulations (dashed lines) and to total soot flux in lake sediment records (solid lines).

Fig. 4: Global changes in the net solar flux at the top of the atmosphere, surface temperature, and precipitation driven by enhanced historical BC emissions (Sens_BC5 - Base).

This figure quantifies the climatic responses to enhanced historical BC emissions by comparing the Sens_BC5 experiment (incorporating increased historical BC background emissions) with the Base experiment (using the standard CMIP7 emission inventory). The left column shows multi-year mean spatial changes in the net solar flux at the top of the atmosphere (FSNTOA) (**a**), surface temperature (**c**), and precipitation (**e**). Positive values indicate increases in the Sens_BC5 experiment relative to the Base experiment. Stippling marks regions where the changes are statistically significant at the 95% confidence level based on a Student's t-test across all simulated years. The right column displays the zonal mean changes for FSNTOA (**b**), surface temperature (**d**), and precipitation (**f**). The black curve represents the zonal mean difference at each latitude, while the red dots indicate the mean values within 30° latitude bands (90°S-60°S, 60°S-30°S, 30°S-0°, 0°-30°N, 30°N-60°N, and 60°N-90°N).

Fig. 5: Seasonal Arctic changes in the net solar flux at the top of the atmosphere, surface net solar flux, and surface temperature driven by enhanced historical BC emissions (Sens_BC5 - Base).

This figure illustrates the seasonal Arctic climatic responses to enhanced historical BC emissions by comparing the Sens_BC5 experiment (incorporating increased historical BC background emissions) with the Base experiment (using the standard CMIP7 emission inventory). The upper figures show spatial distributions of seasonal mean changes in the net solar flux at the top of the atmosphere (FSNTOA) (**a**, **d**, **g**, **j**), surface net solar flux (FSNS) (**b**, **e**, **h**, **k**), and surface temperature (T) (**c**, **f**, **i**, **l**) over the Arctic region. Results are shown for winter (DJF, December-January-February), spring (MAM, March-April-May), summer (JJA, June-July-August), and autumn (SON, September-October-November). Positive values indicate increases in the Sens_BC5 experiment relative to the Base experiment. The bottom figures display the seasonal mean differences averaged over the Arctic region north of 60°N for ΔFSNTOA (**m**), ΔFSNS (**n**), and ΔT (**o**), summarizing the overall seasonal responses in radiative fluxes and surface temperature.

Editorial summary:

Increases in historical black carbon emissions enhanced spring and summer radiative effects north of 60°N, leading to regional surface warming and
accelerated Arctic snowmelt, suggests a study combining climate modeling with lake-sediment records from China.

Peer review information:
Communications Earth and Environment thanks Basudev Swain and the other, anonymous, reviewer(s) for their contribution to the peer review of this work. Primary Handling Editors: Yi Jiao and Nicola Colombo. A peer review file is available.

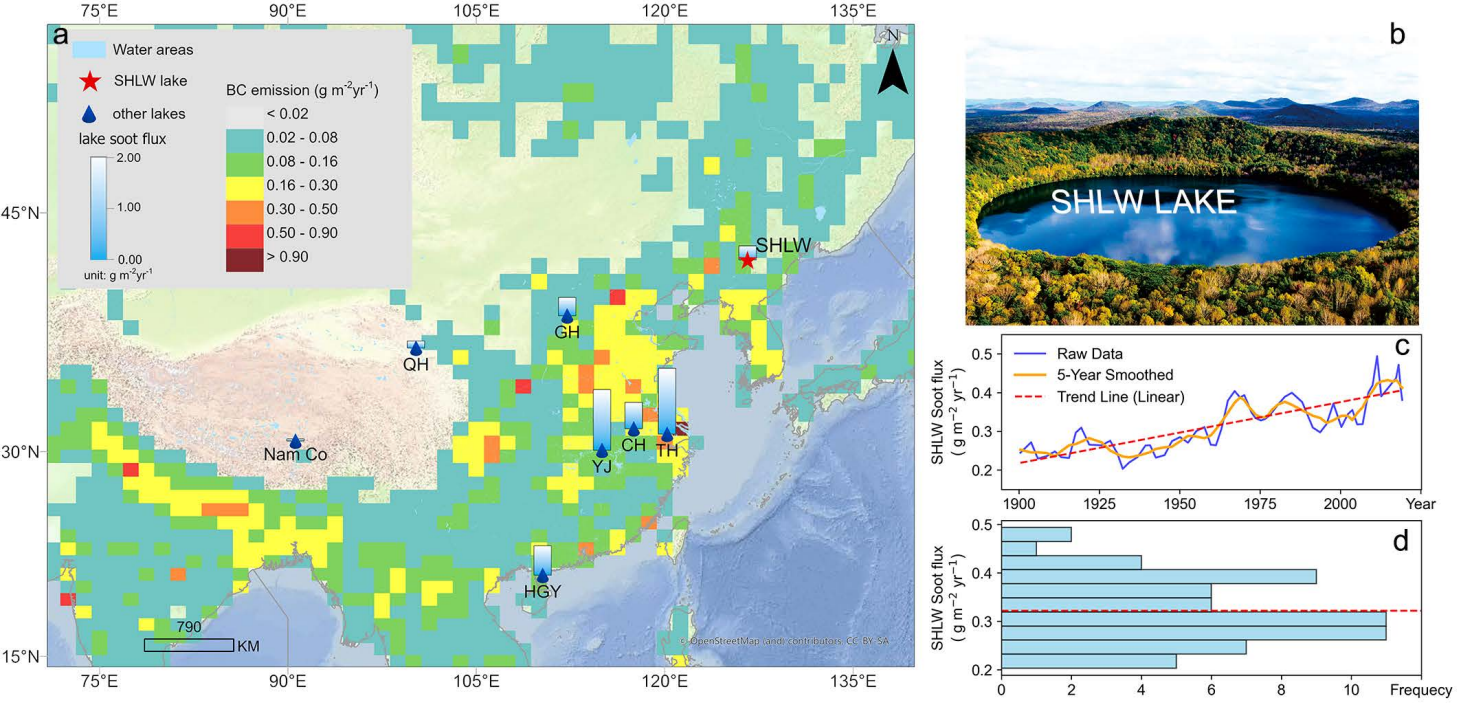

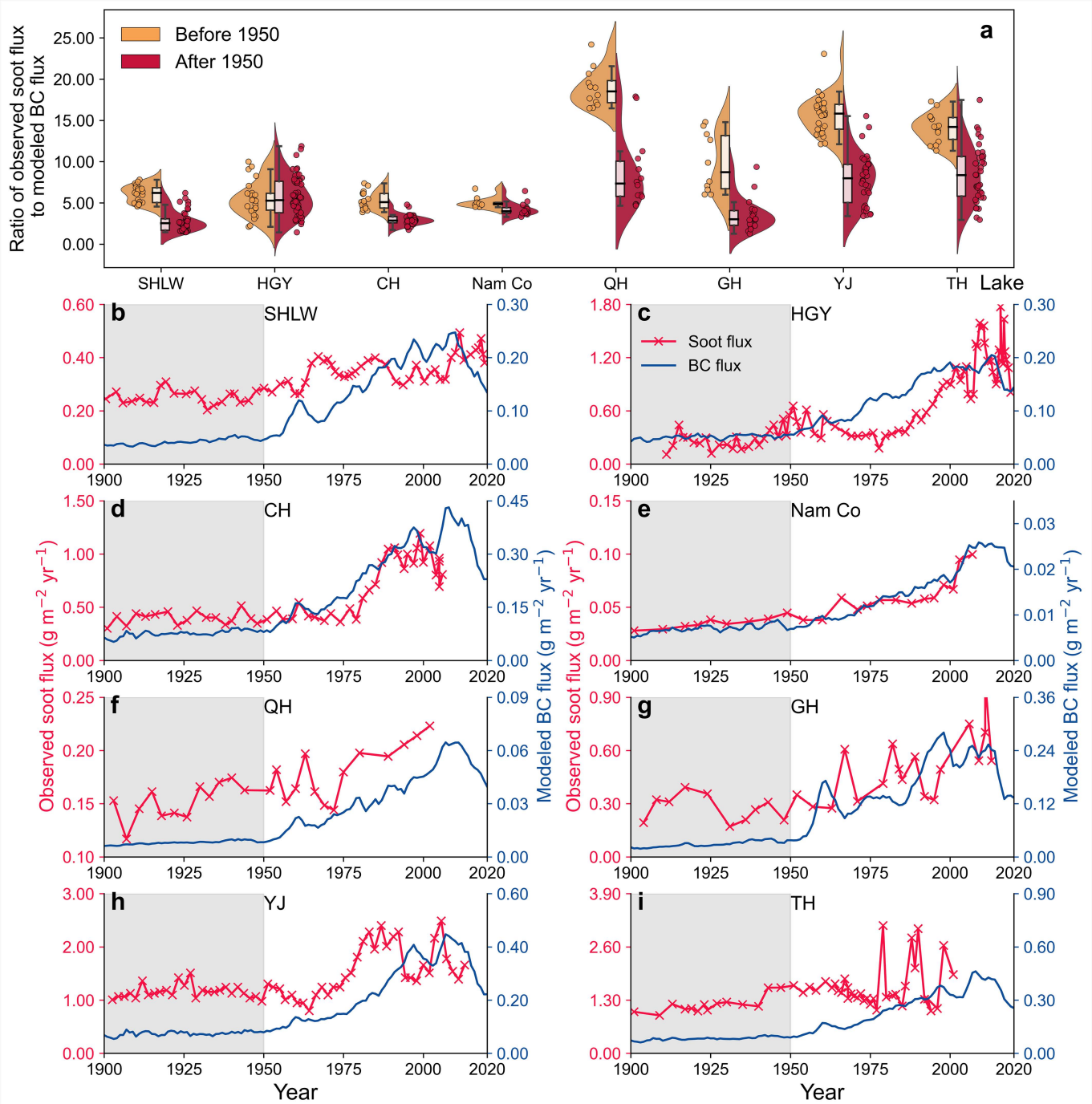
a
Before 1950
After 1950
Ratio of observed soot flux to modeled BC flux
SHLW
HGY
CH
Nam Co
QH
GH
YJ
TH
Lake
b SHLW
c HGY
Soot flux
BC flux
d CH
e Nam Co
f QH
g GH
h YJ
i TH
Observed soot flux (g m−2 yr−1)
Modeled BC flux (g m−2 yr−1)
Year

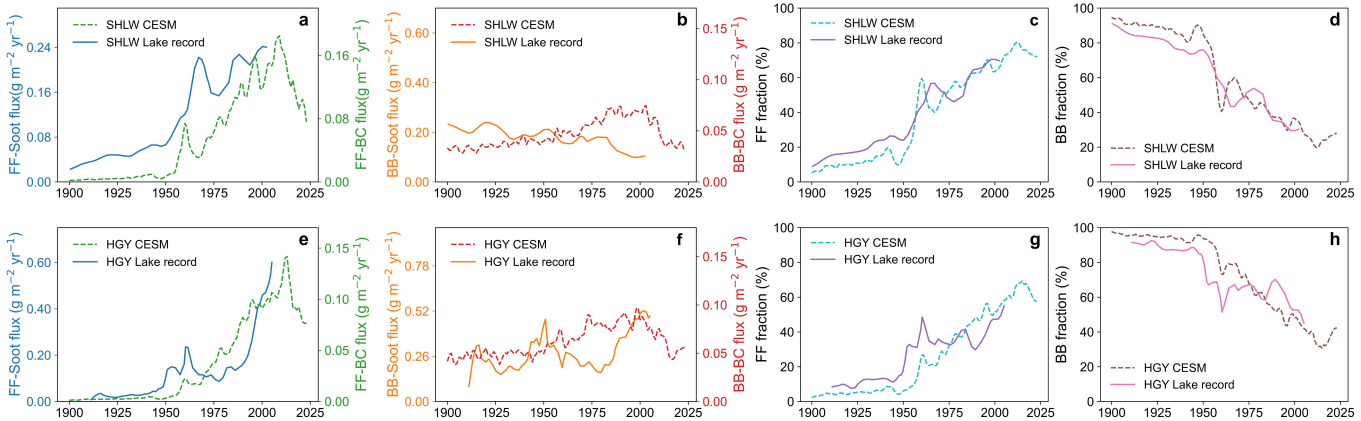

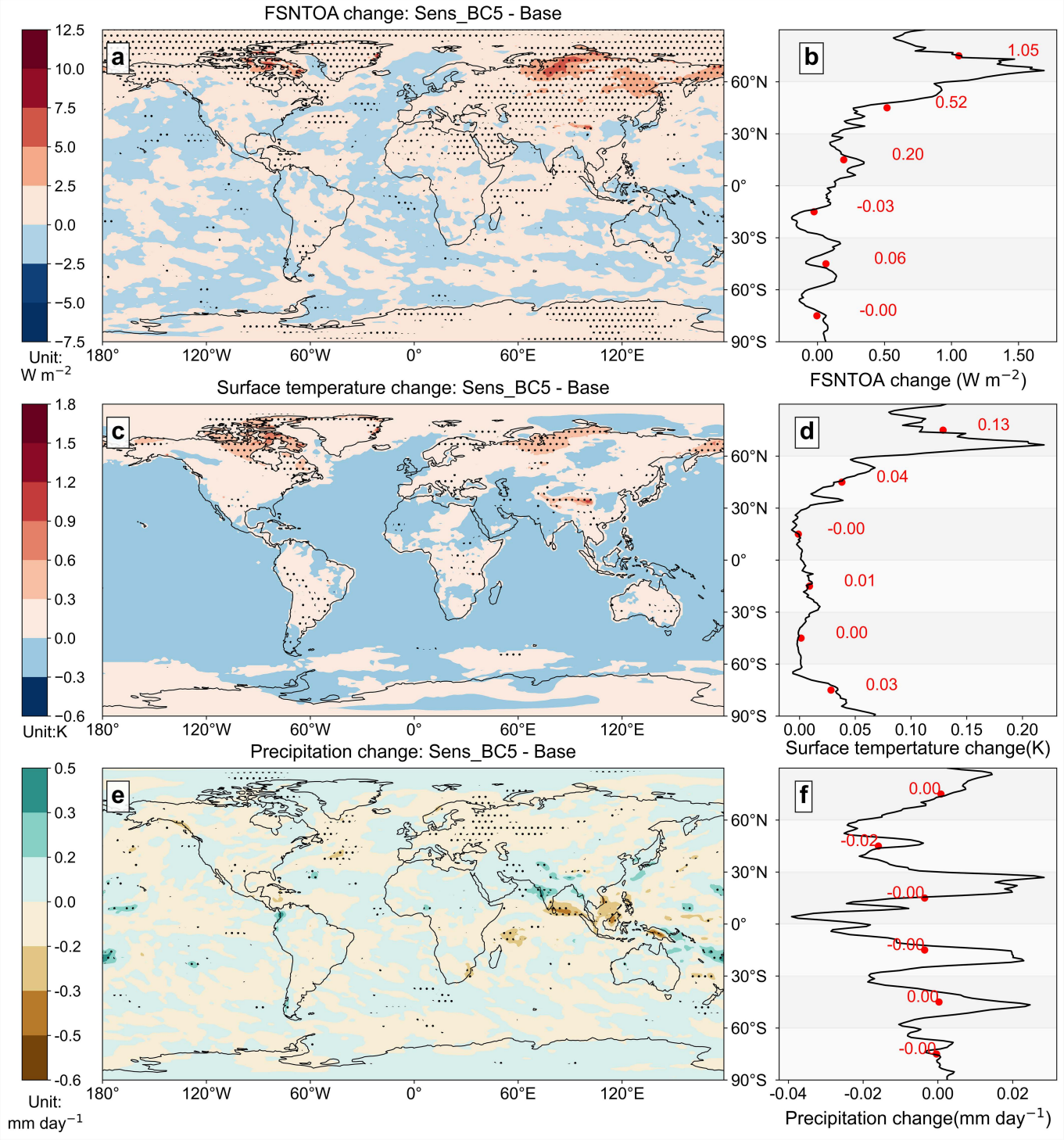
FSNTOA change: Sens_BC5 - Base
a
b
12.5
10.0
7.5
5.0
2.5
0.0
−2.5
−5.0
−7.5
Unit:
W m−2
180°
120°W
60°W
0°
60°E
120°E
60°N
30°N
0°
30°S
60°S
90°S
1.05
0.52
0.20
-0.03
0.06
-0.00
0.00
0.50
1.00
1.50
FSNTOA change (W m−2)
Surface temperature change: Sens_BC5 - Base
c
d
1.8
1.5
1.2
0.9
0.6
0.3
0.0
−0.3
−0.6
Unit:K
0.13
0.04
-0.00
0.01
0.00
0.03
0.00
0.05
0.10
0.15
0.20
Surface tempertature change(K)
Precipitation change: Sens_BC5 - Base
e
f
0.5
0.3
0.2
0.0
-0.2
-0.3
-0.5
-0.6
Unit:
mm day−1
0.00
-0.02
-0.00
-0.00
0.00
-0.00
-0.04
-0.02
0.00
0.02
Precipitation change(mm day−1)

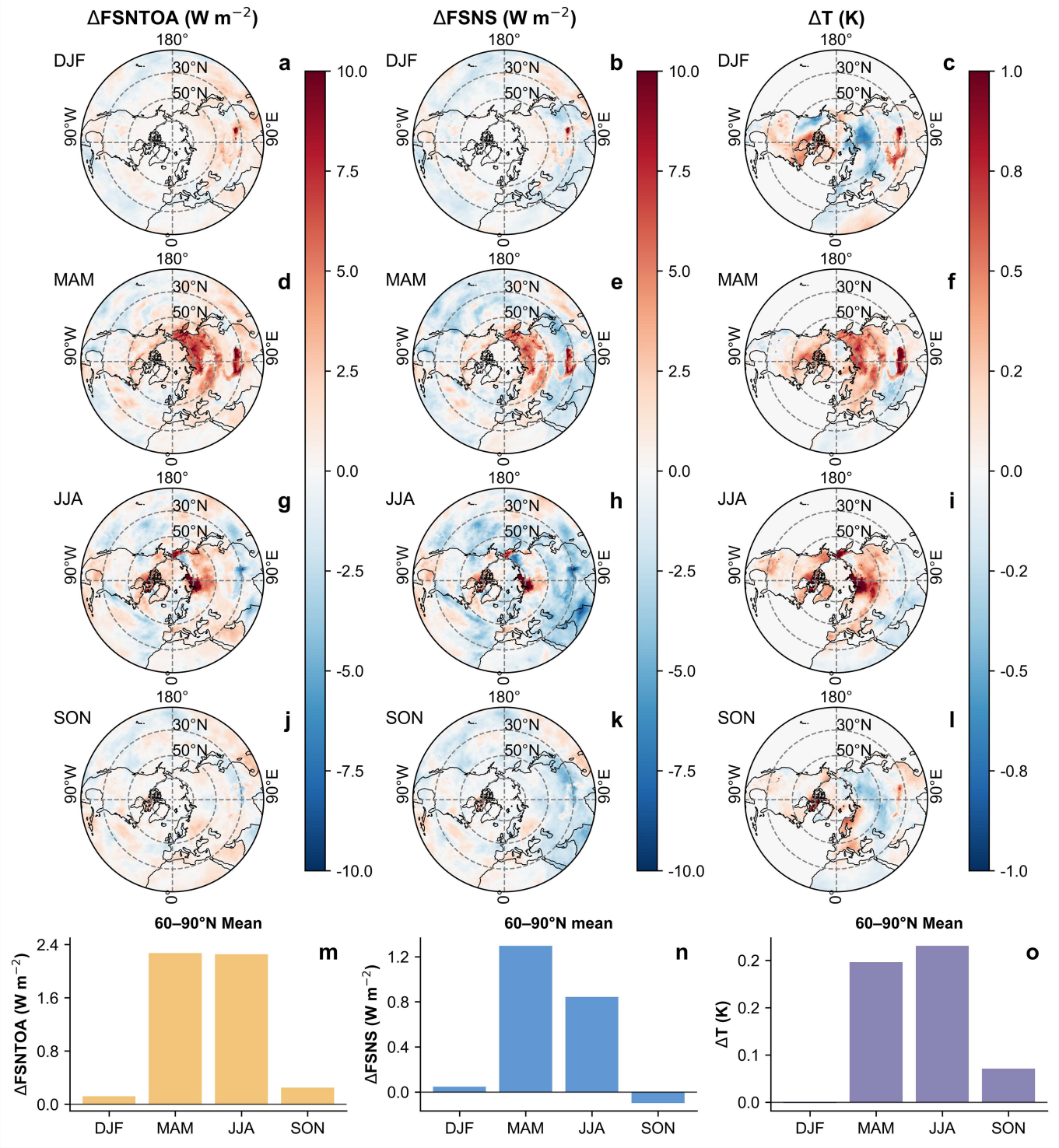
ΔFSNTOA (W m^{-2})
ΔFSNS (W m^{-2})
ΔT (K)
DJF
MAM
JJA
SON
a
b
c
d
e
f
g
h
i
j
k
l
180°
30°N
50°N
90°W
90°E
0°
10.0
7.5
5.0
2.5
0.0
-2.5
-5.0
-7.5
-10.0
1.0
0.8
0.5
0.2
0.0
-0.2
-0.5
-0.8
-1.0
60–90°N Mean
60–90°N mean
60–90°N Mean
m
n
o
ΔFSNTOA (W m^{-2})
ΔFSNS (W m^{-2})
ΔT (K)
2.4
1.6
0.8
0.0
1.2
0.4
0.2
0.1
DJF
MAM
JJA
SON